

The state of the atmosphere throughout the seasons: how well can atmospheric models explain infrasound observations at regional distances

Karl Koch¹ and Christoph Pilger¹

¹BGR

November 22, 2022

Abstract

Over the past two decades the German Aerospace Center facility near Heilbronn, Germany, has conducted a considerable number of tests of the ARIANE-5 main rocket engine. From the 159 studied tests a large portion (~45%) was detected at IMS infrasound station IS26 in the Bavarian forest, located at a distance of about 320 km in an eastward direction (99° clockwise from North). Observations were mostly made during the winter season between October and April with a detection rate of more than 70%, as stratospheric winds then favour atmospheric infrasound propagation within a stratospheric duct. For the summer season the reversal of middle atmospheric wind patterns generally inhibits signal detections, as is found by comparisons of numerical weather prediction models. A significant portion of non-detection cases during winter, however, also exhibit a sound speed profile that should enable infrasound signal observations due to the presence of a stratospheric duct. Using European Centre for Medium-Range Weather Forecast (ECMWF) atmospheric model analysis and infrasound propagation modelling it was found that about two-thirds can be explained by the existence of a shadow zone near the station. For one third of the cases, however, such a shadow zone does not exist and it must be concluded that the applied atmospheric model is more often than expected unable to correctly explain infrasound propagation to regional distances, as has been found in previous studies.

1 **The state of the atmosphere throughout the seasons: how well can atmospheric models**
2 **explain infrasound observations at regional distances**

3

4 Karl Koch, Christoph Pilger

5

6 Federal Institute for Geosciences and Natural Resources

7 Stilleweg 2

8 D-30655 Hannover

9

10

11

12

13

14

15

16

17 **Abstract**

18

19 Over the past two decades the German Aerospace Center facility near Heilbronn, Germany, has
20 conducted a considerable number of tests of the ARIANE-5 main rocket engine. From the 159
21 studied tests a large portion (~45%) was detected at IMS infrasound station IS26 in the
22 Bavarian forest, located at a distance of about 320 km in an eastward direction (99°
23 clockwise from North). Observations were mostly made during the winter season between
24 October and April with a detection rate of more than 70%, as stratospheric winds then favour
25 atmospheric infrasound propagation within a stratospheric duct. For the summer season the
26 reversal of middle atmospheric wind patterns generally inhibits signal detections, as is found
27 by comparisons of numerical weather prediction models. A significant portion of non-
28 detection cases during winter, however, also exhibit a sound speed profile that should enable
29 infrasound signal observations due to the presence of a stratospheric duct. Using European
30 Centre for Medium-Range Weather Forecast (ECMWF) atmospheric model analysis and
31 infrasound propagation modelling it was found that about two-thirds can be explained by the
32 existence of a shadow zone near the station. For one third of the cases, however, such a
33 shadow zone does not exist and it must be concluded that the applied atmospheric model is
34 more often than expected unable to correctly explain infrasound propagation to regional
35 distances, as has been found in previous studies.

36

37

38 Keywords: infrasound, atmospheric models, ground truth source, stratospheric ducting, regional
39 distances, rocket engine tests

40

41 1. Introduction

42 Infrasound signals in the atmosphere from natural and anthropogenic events propagate in a very
43 dynamic and anisotropic medium. Compared to the propagation of seismic waves, the solid earth can
44 be considered a static medium. With the dawn of the Comprehensive Nuclear-Test-Ban Treaty (CTBT),
45 incepted in 1996 after decade-long disarmament negotiations for the monitoring of all environments
46 towards banning nuclear explosion test explosions, the infrasound technology has experienced a
47 rebirth to the research activities in the 1950s and 1960s. Then, atmospheric testing was extensively
48 carried out, but was banned by the LTBT (Limited Test Ban Treaty) in 1963, prohibiting nuclear testing in
49 outer space, under water and in the atmosphere (Dahlman et al, 2010).

50 Numerous studies in recent years (c.f. Le Pichon et al, 2008; Koch, 2010; Green et al., 2011; Fuchs et al.,
51 2019; Koch & Pilger, 2019; Koch & Pilger, 2020) have found examples that the atmospheric specification
52 available from analysis data of numerical weather prediction (NWP) models may not necessarily
53 describe infrasound observations at regional distances adequately enough. In these cases numerical
54 propagation calculations were not always able to predict the observed arrivals, in that the atmospheric
55 models do not include the corresponding duct that is most likely implied to exist based on the wave
56 field parameters extracted from the recorded signals. As initially described by Le Pichon et al. (2008) or
57 Koch (2010) infrasound detection throughout Central Europe is governed by the seasonal switch of the
58 stratospheric wind pattern near the spring and fall equinoxes, with the stratospheric wind pattern
59 pointing towards the east during winter months and reversing during the summer. This consistent
60 pattern has been demonstrated to exist by Koch (2010) who has studied infrasound observations from
61 rocket engine tests carried out for the ARIANE-5 main booster engine for development tests carried out
62 between the years 2000-2004, at a distance of about 300 km at IMS station IS26 to the east-southeast
63 from the source site. In this period infrasound signals from these tests were only observed in the
64 months from November to April, whereas no observations were made during the rest of the year. This
65 observation was further made during a field campaign from late 2011 to May 2012 (Pilger et
66 al., 2013). However, during the campaign we also made an infrasound observation in May 2012, where
67 ray tracing with the European Centre for Medium-Range Weather Forecast (ECMWF) model did not
68 produce an arrival at IS26, except when introducing model variations from gravity wave perturbations
69 (Gardner et al., 1993).

70 In fall of 2018 (3 September) an explosion near Ingolstadt, Southern Germany, provided an impressive
71 number of infrasound observations within a few hundred kilometers providing clear evidence that
72 standard NWP models may fail in specific cases to model infrasound arrivals (Fuchs et al., 2019; Koch &
73 Pilger, 2020). In these cases the model provided strong evidence of sole (or multipathed)
74 thermospheric returns at distances between 200 and 600 km distances, while results from waveform

75 analyses provide strong indications that the observed arrivals were indeed from stratospheric ducting
76 based on obtained estimates of celerity and trace velocity.

77 Other studies (Le Pichon et al., 2015; Hupe et al., 2019) have been conducted in the framework of the
78 Atmospheric Dynamics Research Infrastructure in Europe (ARISE) project (Blanc et al., 2018) and were
79 aimed at assessing the accuracy of middle atmosphere numerical weather prediction models, e.g.,
80 from ECMWF. In these studies model data from ECMWF were compared to estimates of temperature
81 and wind speed components from satellite and ground based observation systems. Le Pichon et al.
82 (2015) found from lidar and wind radiometer measurements at the OHP observatory that results are
83 broadly consistent with the ECMWF model for altitudes up to ~ 40 km, but differences become
84 significant for greater heights, with differences exceeding 5°K for temperature and 20m/s for zonal
85 wind. Hupe et al (2019) investigated the temperature field of ECMWF models with the temperature
86 field from Compact Rayleigh Autonomous Lidar measurements which indicated a cold bias above 40
87 km with a maximum near 60 km altitude of about 12K , with two standard deviations of $4.5\text{-}6^\circ\text{K}$. They
88 also evaluated the impact on the detection pattern for microbaroms after inclusion of uncertainties in
89 temperature and horizontal winds and found a significant improvement compared to the direct output
90 of the ECMWF model.

91 Since the German Aerospace Center (Deutsches Zentrum für Luft- und Raumfahrt/DLR) facility near
92 Heilbronn, Germany, has conducted a considerable number of tests of the ARIANE-5 main engine over
93 the past two decades, we take here the opportunity of a large ground-truth dataset of about 160
94 rocket engine tests to investigate the adequacy of the ECMWF models in correctly predicting arrivals or
95 non-arrivals at station IS26 in the Bavarian Forest (see also Figure 1). In particular we focus on those
96 cases where we lack an observation when an arrival is predicted, and on other cases when arrivals exist
97 but the model fails to predict them. The distance range of 300 km is of particular interest since it
98 normally partitions the range of tropospheric wave propagation from the range where atmospheric
99 infrasound starts to show stratospheric ducting, with both ranges being separated by an acoustic
100 shadow zone (Gutenberg, 1939). As to how prominent this shadow zone impacts on non-detections
101 will further be studied.

102 As detailed below, this study is significantly different in scope from the recent study by Pilger et al.
103 (2021), where the infrasonic signature of 1001 rocket launches, including 66 ARIANE-5 rockets,
104 were investigated. While long-range infrasound detectability of this type of rocket was clearly proven
105 there, the present study aims primarily at regional infrasound propagation and at a different ARIANE 5
106 source configuration. Firstly, we study here infrasound emitted from the main engine, while in the
107 previous study additional booster stages are involved. And secondly, we deal in this study with a

108 spatially fixed ground-truth source, while Pilger et al. consider a laterally and vertically moving
109 infrasound source along its flight path.

110

111

112 2. The ground-truth source and its location from the receiver

113 The ground truth source being used for this study is the one already described by Koch (2010), and
114 which was further the subject of Pilger et al.'s (2013) study. In the 1990s, the Space Propulsion
115 Institute of DLR at Lampoldshausen near Heilbronn, Southern Germany, established a testing facility
116 (called P5) within the development programme for the ARIANE-5 main engine. This facility is located
117 at latitude 49.3°N and longitude 9.4°E (Figure 1). While in the early years, up to 2004, the purpose of
118 the facility was testing of the design concepts for the VULCAIN I and II engines, the testing later
119 shifted to acceptance testing before use in the space flight programme of the European Space Agency
120 (ESA), which has continued to the present. For each test the main engine of ARIANE-5 with a thrust of
121 1000 kN is mounted in the P5 facility and, hence, provides fairly identical setups for each test,
122 including the deflection of the propulsion jet towards the southeast, approximately in the direction
123 to the infrasound array station IS26 recording the atmospheric pressure waves. Therefore we assume
124 that the infrasound generation mechanism is nearly identical from test to test and that regional
125 infrasound observations are, for the most part, governed by the atmospheric parameters at the times
126 of the tests.

127 As shown in Figure 1, IMS station IS26 is located at an azimuth of $\sim 100^\circ$ and a distance of ~ 320 km
128 from Lampoldshausen. With known test duration and the theoretical backazimuth of 282° , two
129 parameters are available to reliably identify the infrasound signal in the observations: (1) the signal
130 duration in the waveforms and (2) the backazimuth from array processing techniques are to be
131 matched when declaring detection. From 2000 to 2019 we received the ground-truth parameters
132 (date & time, test duration) for more than 170 engine tests by DLR, of which about a dozen had
133 durations of less than 10 seconds, while nearly 100 tests lasted more than 600 seconds (10 mins),
134 being considered the minimum thrusting time of this stage for a successful rocket launch. From all
135 tests, nearly 100 were carried out during the initial five years starting in 2000 (Koch, 2010), whereas
136 for another set of more than 70 tests over the subsequent 15 years the ground-truth information was
137 collected recently (K. Fröhlke, pers. communication). Only for one test the corresponding waveform
138 data could not be found in our data archive.

139

140 3. Data analysis

141 With the distance of 320 km between IS26 and Lampoldshausen and celerities of tropospheric
142 acoustic waves of 320-350 m/s (Negraru et al., 2010), such waves would arrive between 15 and 16
143 min after the propulsion test's origin time, while stratospheric waves with celerities of 280-320 m/s
144 would arrive another 2mins later. Within these delay time windows an interactive search for
145 corresponding signal onsets was carried out. When the signal could be identified, mainly based on
146 the signal duration corresponding to the propulsion duration, a frequency-wavenumber (F-K) analysis
147 (Stammler, 1993) was carried out to find the backazimuth and the apparent velocity (or slowness). In
148 most cases a signal could be identified, reflecting the theoretical backazimuth within a few degrees.

149 In Figure 2 the waveforms are shown for a couple of events that were detected at IS26 with different
150 signal to noise ratios (SNR). The data are filtered with a high-pass filter of 2 Hz. The frequency range
151 considered in this study is therefore beyond the frequency band commonly considered in infrasound
152 studies based on IMS stations, ranging between a few seconds period and several Hz (Campus, 2004;
153 Campus & Christie, 2010). The waveforms of the upper two events, where signals above 3 Hz clearly
154 stand out from the background noise, represent data with a rather decent SNR of about 3 to 5. The
155 third event shows more emergent, and hence less prominent, waveforms with a SNR of between 1
156 and 2. The lower waveforms are from two events that do not exhibit any engine test signals, but only
157 noise bursts or signals of no interest. One case is from a propulsion test in winter (Dec 2000), where
158 atmospheric ducting conditions between the DLR facility and IS26 are usually favourable; while for
159 the second case of a test in summer (July 2001) the propagation conditions normally do not allow the
160 observation of a signal.

161 As previously found for Central Europe, pressure sources west of infrasound stations lead to frequent
162 infrasound detections from fall to spring equinoxes, while signal detections are prominent from the
163 opposite direction during summer months (Le Pichon et al., 2008; Koch, 2010; Green et al., 2011;
164 Gibbons et al., 2015; Pilger et al., 2018). Figure 3 as well as Table 1 summarize the detection statistics
165 for all 159 ARIANE engine tests from 2000 to 2019 as observed at IS26, and hence follow this pattern.
166 In this compilation all tests of duration less than 10 sec were left out, as they may not have been
167 easily identified due to the short duration or an inability to obtain stable F-K analysis results. Except
168 for a single observation each in May and September all other 69 tests yielding infrasound signals
169 occurred only from October to April, where a majority of all conducted engine tests could be
170 detected; only one quarter of the tests in these winter months resulted in non-detections at
171 IS26. Non-detections in the summer months May to September are pervading, i.e. for 63 (97%) out of
172 65 engine tests in the summer season it was not possible to find an associated signal.

173 For each identified infrasound signal a frequency-wavenumber analysis was carried out. The raw
174 waveform data were high-pass filtered with 2 or 3 Hz, depending on the optimal signal, and a
175 frequency wavenumber analysis was carried out for frequencies up to 6 Hz. A maximum slowness
176 range of 450 s/deg was applied with a discretization of 120 points, as required by the analysis
177 program (Stammler, 1993), covering trace velocities down to 250 m/s. The associated results
178 gathered for backazimuth, slowness and apparent velocity are displayed in Figure 4. The theoretical
179 backazimuth from IS26 to Lampoldshausen is well represented with azimuths scattering with about 5-
180 6 ° with respect to the expected value of 282°. For slowness we obtained mostly values between
181 300-340 s/deg, translating into trace velocities between 330 and 370 m/s. These values indicate
182 therefore stratospheric ducting, as they appear to exceed the near surface sound velocities of 330-
183 340 m/s. In Figure 4 a stronger scatter in the estimated array processing results seems to occur prior
184 to 2008 which may be related to the upgrade from a five-element to an eight-element infrasound
185 array, providing more stable array processing results.

186 In order to assess the fraction of non-detections that may be due to increased background noise
187 levels at the IS26 array we present signal vs. noise levels for detections and only noise levels for the
188 cases of non-detections from element I26H1, as shown in Figure 5. For identified signals the
189 estimation was carried out in windows being representative. They were set such to include, if
190 possible, the entire signal, but in the presence of spikes or noise bursts to exclude them. Noise signal
191 estimates were made immediately preceding the signal window. In the case of non-detections the
192 amplitude window was selected within the expected arrival time window. As signal and noise level
193 measure the root-mean-squares (RMS) amplitude was taken, considered a stable amplitude estimate
194 in the presence of incidental noise, such as spikes or bursts. First it is noted that noise levels prior to
195 2005 are somewhat higher than for later years, probably by some 50%. This effect should be
196 associated with the noise reduction filter system at IS26, which was upgraded with impedance filters
197 attached to the pipe outlets during 2004. In Koch (2010) signal levels at all elements of IS26 were
198 assessed for the years 2000-2004 with a decrease found for I26H4 in 2003 when this element was
199 equipped temporarily with such impedance reducers in a test to suppress spurious spectral peaks
200 caused by the spatial noise reduction system used at IS26.

201 While noise levels are mostly below 0.015 amplitude units prior to 2005, the noise levels after 2004
202 are below 0.01 amplitude units. From this result, we conclude that non-detections with noise levels
203 above this baseline level may not be found due to an insufficient signal-to-noise ratio. Of course, the
204 opposite conjecture may also hold: events with pre-event signal levels (i.e. noise) below the baseline
205 should be detected.

206

207 4. Numerical weather prediction models

208 As is well known (LePichon et al., 2015) atmospheric conditions are significantly different between
209 spring and fall equinoxes, in particular with respect to the reversal of the dominant stratospheric wind
210 direction. The particular atmospheric models considered here are based on the ECMWF atmospheric
211 specification for altitudes up to 60-70 km which is then extended to greater heights by smooth
212 transition to the climatological models HWM14 and MSISE00 (Drob et al., 2015; Picone et al., 2002).
213 From the ECMWF models the six-hour analysis data were used including the physical parameters
214 pressure, temperature and wind speeds. The model reference is established as a 1-D effective sound
215 speed model at the midpoint between source (DLR) and receiver (IS26), geographically lying near the
216 center of a triangle outlined by the cities of Nuremberg, Regensburg and Ingolstadt, while for the
217 raytracing modeling we apply a 2D atmospheric model along the source receiver path.

218 The resulting models applicable for each ARIANE-5 engine test in the last 20 years for the cases with
219 signal detections and cases with non-detections are examined and compared for gross specific features
220 to explain the differences in observations (Figure 6). The 1D reference model is considered a good
221 characterization of the atmospheric state, as the west-to-east conditions are quite stable over the
222 distance range of 300km between source and receiver. All ECMWF reference models for the detection
223 cases (Figure 6a) show a distinct maximum in effective sound speed leading to a strong stratospheric
224 duct for altitudes between 40 and 60 km. This similarity of the atmospheric models is clearly reflected
225 in the mean model and median model, which are closely matching. It further finds its expression in the
226 standard deviation curves yielding an effective sound speed ratio, i.e. the ratio of the effective sound
227 speed at stratospheric heights to the one near the ground, being above a value of 1, which, according
228 to Le Pichon et al. (2012) represents a sufficient condition for stratospheric ducting. The ECMWF
229 models for the non-detection cases (Figure 6b) show a contrasting picture, with most models not
230 showing an effective sound-speed peak for stratospheric heights, therefore not enabling stratospheric
231 ducting. This is, of course, reflected in the mean and median models which do not reach effective
232 sound speed ratios of 1 and therefore explain well the non-observations. However, it is also shown that
233 a considerable portion of atmospheric models for the cases of non-detections indicate the presence of
234 a stratospheric duct with the potential for stratospheric arrivals; this dissimilarity with the majority of
235 background models is therefore reflected in the clear mismatch between the mean and median models
236 and the positive standard deviation curve. This latter curve also exhibits a sound speed ratio of larger
237 than 1.

238 In Figures 7 histograms of the resulting effective sound speed ratios ($v_{\text{eff-ratio}}$) from the ECMWF model
239 applying for infrasound detections and non-detections at the times of ARIANE-5 tests are displayed.
240 The quantity shown is defined here as the ratio of the maximum effective sound speed in the altitude

241 range of 30 to 70 km to the maximum sound speed in the lower 5 km above the ground. For the 71
242 detections (Fig.7a) all but four showed ratios above 1, with the remaining ones falling short of this
243 value by less than 1.5%. For the non-detections (Fig.7b) about one quarter of cases (20) shows
244 effective sound speed ratios exceeding the enabling value of 1. These cases therefore deserve further
245 discussion below.

246 Additional examination of the effective sound speed ratios over the seasons (Fig.8) in relation to
247 allowed detections or not reveals an interesting, even though expected, pattern for winter and summer
248 months (Le Pichon et al., 2008; Koch, 2010). Near the times of the equinoxes the $v_{\text{eff-ratio}}$ changes from
249 values above 1 to values below 0.9. The most striking part is in particular the rather small scatter in the
250 considered quantity during the summer, while the scatter can be on the order of 40-50% during the
251 winter. In other words, the rather low variability of the effective sound speed ratios in the summer
252 season explains the consistent lack of detections during this time. As effective sound speed is
253 dominated by temperature and wind speeds, the strong scatter during winter is an expression of a
254 higher variability of these parameters during winter between near-ground troposphere and middle
255 atmosphere (stratosphere).

256 To further investigate the probability of signal detection for high $v_{\text{eff-ratio}}$ and to identify an underlying
257 pattern Table 2 list the numbers of detections and non-detections depending on the $v_{\text{eff-ratio}}$ ordered in
258 various ranges, namely >1.2, 1.1-1.2, 1.0-1.1, 0.98-1.0, and <0.98. The last class does not contain any
259 detection, as is also indicated in Figs.7 and 8. In this table we give three different quality levels for the
260 detections in terms of their signal strength and variability: (2) good, (1) weak, and (0) poor where good
261 signal conditions indicate a SNR above 2-3 and weak and poor conditions those below 2; poor signals
262 furthermore show instable signal content. In each column of the table we give two numbers depending
263 on whether the atmospheric model shows a shadow zone or not, i.e., when a stratospheric duct can be
264 expected to exist (for $v_{\text{eff-ratio}} > 1$ or > 0.98 when counting on gravity wave influences, respectively; see
265 e.g. Pilger et al., 2013). Of the 36 cases with highest $v_{\text{eff-ratio}}$, i.e. >1.2, the overwhelming number of
266 cases (~70%) consist of clear detections, with a few cases of weaker signals including very few cases of
267 shadow zones, but also 5 cases (14%) of non-detections where only in one case a shadow zone is
268 predicted for IS26, i.e. the range of about 320 km. For the next two categories of smaller $v_{\text{eff-ratio}}$, but
269 still above 1, the number of detections with good signals decreases rapidly, but is somewhat
270 compensated by detections with lesser signal levels, while the non-detections reach proportions of
271 about 30%. In most of these cases the atmospheric model produces a shadow zone explaining well the
272 absence of signals.

273 With the 25 detections for which the ECMWF and propagation modeling unambiguously predicts
274 shadow zones and the 7 non-detections without an associated shadow zone (see Table2), we then find

275 32 cases of ARIANE tests that are not adequately dealt with by the atmospheric modeling in terms of
276 the signal prediction by stratospherically ducted waves. A similar case has been seen for the Ingolstadt
277 explosion, where both Fuchs et al. (2019) and Koch & Pilger (2020) identified clear stratospheric
278 arrivals in cases where the ECMWF model was not able to produce them. Both studies therefore
279 suggest that failure to predict stratospheric arrivals at regional distances is absolutely not a rare case,
280 but can occur on the order of 20 percent of the cases. Of course, some of the cases with IS26 being
281 actually or possibly within a stratospheric shadow zone could be treated within the framework of
282 dynamic gravity wave coupling (Gardner et al.,1993). Such modification explains well the occurrence of
283 a detection for the test on 14 May 2012, where the ECMWF model alone predicts a shadow zone, as
284 studied by Pilger et al. (2013).

285 For quantifying the rate of the ECMWF model potentially failing to predict a signal detection at IS26
286 from the ARIANE tests, we can consider the 46 correctly predicted arrivals from propagation modeling
287 with the 25 detections without success (see Table 2); hence, we get approximately a 1:2 chance of not
288 being able to predict the correct propagation result.

289 For the case for $0.98 < v_{\text{eff-ratio}} < 1$, where we are relatively close to the case of stratospheric ducting, we
290 obtain a surprisingly similar result when a 4:9 chance of detection versus non-detection is found. And
291 finally we have the case of 20 non-detections (i.e. for $v_{\text{eff-ratio}} > 1$, see also Table3), of which 13 are
292 explained by shadow zones, but 7 are not. Again we have a 1:2 chance of not explaining an observation
293 correctly.

294

295 **5. Investigations on cases of interest**

296 Of specific interest in the interpretation of infrasound from the ARIANE-5 rocket engine tests are the
297 cases where the $v_{\text{eff-ratio}}$ enables a stratospheric duct in general, but when a receiver can still not detect
298 a stratospheric arrival. In this scenario we presume that the stratosphere is equally transparent to
299 atmospheric waves over a larger frequency range, which is mostly the case (Sutherland & Bass, 2004,
300 Waxler et al., 2017a). Often such scenarios then arise when the atmospheric models are such that the
301 range and location of associated shadows zones (or zones of silence; Gutenberg, 1939) varies largely
302 and is particularly pronounced at regional distance, so that detections or non-detections may occur on
303 a case by case basis at a specific range like the 320 km distance studied here.

304 As has been found (see Table 2) there are 20 cases of ARIANE tests(see Table 3for a list of these cases),
305 where no signal could be identified in the IS26 waveform data, even though stratospheric ducting
306 follows from the $v_{\text{eff-ratio}} > 1$. While 13 of these tests are associated with a shadow zone according to the

307 ECMWF model, the remaining 7 tests do not exhibit such a zone; thus signals are expected to occur, as
308 is demonstrated in Figure 9. The propagation modeling has been carried out with a 2D raytracing code
309 (Margrave and Lamoureux, 2019) and according 2D atmospheric background profiles. The modelling
310 shows, as expected from the effective sound speed ratio, a suitable stratospheric duct and rays
311 bouncing between the ground and the middle atmosphere. In all 7 cases, we see a stratospheric
312 shadow zone to distances up to 120-150 km distance with an occasional second shadow zone at twice
313 this distance. However, for the relevant distance of IS26 beyond 300 km in all of the demonstrated
314 cases an eigenray exists between source and receiver.

315 Lastly, while gravity wave perturbation have proven to be effective in explaining detections within
316 shadow zones, because the fine structure introduced within the stratospheric model often enables
317 eigenrays to reach recording stations that are otherwise missed (e.g. Pilger et al., 2013), we have not
318 seen the opposite case. This can be explained by the tendency of this approach not necessarily to shift
319 a shadow zone, but rather to narrow it, so that stations close to shadow zone boundaries are reached
320 by eigenrays. A similar argument can also be made for the case of parabolic equation modelling
321 (Waxler et al., 2017b), with its ability to illuminate regions, for which ray tracing cannot provide
322 adequate eigenrays.

323

324 **6. Discussion and conclusions**

325 Over two decades, or annual seasons, a repeatable infrasound ground truth source, providing a
326 consistent and controlled environment compared to the case of other sources of infrasound such as
327 rocket launches (Pilger et al., 2021) or accidental explosions (cf. Campus, 2004; Campus & Christie,
328 2010) has been observed by IMS station IS26 at a regional distance of about 320 km. Within this
329 distance stratospheric wave propagation develops including the occurrence of acoustic shadow zones.
330 This phenomenon has therefore been observed over a larger range of atmospheric states and is clearly
331 reflected by the two main seasons, summer and winter, being divided by the spring and fall equinoxes.

332 With the large number of 159 test events we have studied here our ability of detecting infrasound
333 signals from the ground truth source and how it correlates with the development of a stratospheric
334 duct. This duct is consistently absent for the path considered, from west-northwest to east-southeast,
335 for the summer months, as reflected by a fairly stable effective sound speed ratio below 0.9. During
336 equinox times this ratio changes regularly in time to values above 0.95 and mostly above 1.0 enabling
337 stratospheric wave propagation. However, in winter months the effective sound speed ratio is highly
338 variable reaching values up to 1.4-1.5. Even though stratospheric ducting is thus given in principle, it
339 does not necessarily lead to waves that reach an infrasound station, if it is located in a shadow zone.

340 Therefore, of the nearly 90 cases with suitable atmospheric states to observe a stratospheric arrival, we
341 find 20 cases without signal detection at IS26. While two thirds of these cases can be attributed to the
342 occurrence of an acoustic shadow zone, we find a substantial portion, where the atmospheric model
343 fails to produce a shadow zone and therefore failing to explain the arrival. In these cases, however, we
344 do not observe increased levels of background noise.

345 In general, for the 71 detections out of the 159 tests we note that at least 25 observations were made
346 for cases with the ECMWF model showing a shadow zone. With the previous finding we can
347 hypothesize that for regional infrasound propagation we should expect in about 30% of cases that the
348 modeling will not be able to explain the signal at hand, if it is expected to have a stratospheric
349 propagation path. Such a finding is supported by recent studies of Fuchs et al. (2019) and Koch & Pilger
350 (2020) for an explosion source in the same general area of Central Europe, where strong evidence for
351 stratospheric arrivals was found, but propagation modeling failed to support these findings.

352

353

354 **Acknowledgements and Data Availability Statement**

355 This research was carried out within the German National Data Centre activities based on its mandate
356 towards verification of the Comprehensive Nuclear-Test-Ban Treaty (CTBT). Atmospheric model data
357 were retrieved from the European Centre for Medium-Range Weather Forecasts (ECMWF), see
358 www.ecmwf.int. The infrasound data of IS26 are available from the BGR archive at the International
359 Federation of Digital Seismograph Networks (FDSN) data centers, accessible via
360 www.fdsn.org/datacenters/.

361

362 **References**

363

364 Blanc, E. et al., 2018. Toward an improved representation of middle atmospheric dynamics thanks to
365 the ARISE project, *Surv. Geophys.*, 39, 171–225.

366 Campus, P. (2004). The IMS infrasound network and its potential for detection of events: examples of
367 a variety of signals recorded around the world, *InfraMatics*, 6, 13-22.

368 Campus, P. and D. Christie (2010), Worldwide observations of infrasonic waves, in: Le Pichon, A., E.
369 Blanc, and A. Hauchecorne (Eds.), *Infrasound Monitoring for Atmospheric Studies*, Springer,
370 Heidelberg, Germany. ISBN: 978-1-4020-9507-8, p.185-234.

371 Dahlman, O., S. Mykkeltveit & H. Haak (2009). Nuclear test ban: converting political visions to reality,
372 Springer Netherlands, pp. 250, ISBN: 978-1-4020-6883-6, doi: 10.1007/978-1-4020-6885-0.

373 Drob, D.P., J.T. Emmert, J.W. Meriwether, J.J. Makela, E. Doornbos, M. Conde, G. Hernandez, J. Noto,
374 K.A. Zawdie, S.E. McDonald, J.D. Huba, J.H. Klenzing (2015). An update to the Horizontal Wind Model
375 (HWM): the quiet time thermosphere, *Earth and Space Science*, 2, 301-319, doi:
376 10.1002/2014EA000089.

377 Fuchs, F., F. M. Schneider, P. Kolinsky, S. Serafin & G. Bokelmann(2019). Rich observations of local and
378 regional infrasound phases made by the AlpArray seismic network after refinery explosion. *Scientific*
379 *Reports*, 9, 13027, doi: 10.1038/s41598-019-49494-2.

380 Gardner, C.S., C.A. Hostetler & S.J. Franke (1993). Gravity wave models for the horizontal wave
381 number spectra of atmospheric velocity and density fluctuations, *J. Geophys. Res.*, 98, 1035-1049,
382 doi: 10.1029/92JD02051.

383 Gibbons, S.J., V. Asming, L. Eliasson, A. Fedorov, J. Fyen, J. Kero, E. Kozlovskaya, T. Kværna, L. Liszka,
384 S.P. Näsholm, T. Raita, M. Roth, Y. Vinogradov (2015). The European Arctic: a laboratory for
385 seismoacoustic studies, *Seism. Res. Lett.*, 86, 917–928, doi: 10.1785/0220140230.

386 Green, D.N., J. Vergoz, R. Gibson, A. Le Pichon & L. Ceranna (2011). Infrasound radiated by the Gerdec
387 and Chelophechene explosions: propagation along unexpected paths, *Geophys. J. Int.*, 185, 890–910,
388 doi: 10.1111/j.1365-246X.2011.04975.x.

389 Gutenberg, B. (1939). The velocity of sound waves and the temperature in the stratosphere in
390 Southern California, *Bull. Amer. Met. Soc.*, 20, 192-201.

391 Hupe, P., L. Ceranna, C. Pilger, M. de Carlo, A. Le Pichon, B. Kaifler & M. Rapp (2019). Assessing the
392 middle atmosphere weather models using infrasound detections from microbaroms, *Geophys. J. Int.*,
393 216, 1761-1767, doi: 19.1093/gji/ggy520.

394 Koch, K. (2010). Analysis of signals from an unique ground-truth infrasound source observed at IMS
395 station IS26 in Southern Germany, *Pure Appl. Geophys.*, 167, 401-412.

396 Koch, K. & C. Pilger (2019). Infrasound observations from the site of past underground nuclear
397 explosions in North Korea, *Geophys. J. Int.*, 216, 182–200, doi: 10.1093/gji/ggy381.

398 Koch, K. & C. Pilger (2020). A comprehensive study of infrasound signals detected from the Ingolstadt,
399 Germany, explosion of 1 September 2018, *Pure Appl. Geophys.*, 177, 4229, doi: 10.1007/s00024-020-
400 02442-y

401 Le Pichon, A., J. Vergoz, P. Herry & L. Ceranna (2008). Analyzing the detection capability of infrasound
402 arrays in Central Europe, *J. Geophys. Res.* 113, D12115.

403 Le Pichon, A., L. Ceranna & J. Vergoz (2012). Incorporating numerical modeling into estimates of the
404 detection capability of the IMS infrasound network, *J. Geophys. Res.*, 117, D05121, doi:
405 10.1029/2011JD016670.

406 Le Pichon, A., J.D. Assink, P. Heinrich, E. Blanc, A. Charlton-Perez, C. F. Lee, P. Keckhut, A. Hauchecorne,
407 R. Rüfenacht, N. Kämpfer, D. P. Drob, P. S. M. Smets, L. G. Evers, L. Ceranna, C. Pilger, O. Ross & C.
408 Claud (2015). Comparison of co-located independent ground-based middle atmospheric wind and
409 temperature measurements with numerical weather prediction models, *J. Geophys. Res. Atmos.*, 120,
410 8318–8331, doi: 10.1002/2015JD023273.

411 Margrave, G.F. & M.P. Lamoureux (2019). *Numerical methods of exploration seismology - with*
412 *algorithms in MATLAB®*, Cambridge University Press, ISBN: 9781316756041, doi:
413 10.1017/9781316756041.

414 Negraru, P. T., P. Golden & E. T. Herrin (2010). Infrasound propagation in the "Zone of Silence",
415 *Seismol. Res. Lett.*, 81, 614-624, doi: 10.1785/gssrl.81.4.614.

416 Picone, J. M., A. E. Hedin, D. P. Drob & A. C. Aikin (2002). NRLMSISE-00 empirical model of the
417 atmosphere: statistical comparisons and scientific issues, *J. Geophys. Res.*, 107 (A12), 1468, doi:
418 10.1029/2002JA009430.

419 Pilger, C., F. Streicher, L. Ceranna & K. Koch (2013). Application of propagation modeling to verify and
420 discriminate ground-truth infrasound signals at regional distances, *Inframatics*, 2, 39-55, doi:
421 10.4236/inframatics.2013.24004.

422 Pilger, C., L. Ceranna, J. O. Ross, J. Vergoz, A. Le Pichon, N. Brachet, E. Blanc, J. Kero, L. Liszka, S.
423 Gibbons, T. Kvaerna, S.P. Näsholm, E. Marchetti, M. Ripepe, P. Smets, L. Evers, D. Ghica, C. Ionescu, T.
424 Sindelarova, Y. Ben Horin & P. Mialle(2018). The European Infrasound Bulletin, *Pure Appl.Geophys.*,
425 175, 3619–3638, doi:10.1007/s00024-018-1900-3.

426 Pilger, C., P. Hupe, P. Gaebler & L. Ceranna (2021). 1001 rocket launches for space missions and their
427 infrasonic signature, *Geophys. Res. Lett.*, 48, e2020GL092262, doi: 10.1029/2020GL092262

428 Stammer, K. (1993). SeismicHandler—Programmable multichannel data handler for interactive and
429 automatic processing of seismological analyses, *Computers and Geosci.* 19, 135–140.

430 Sutherland, L. C & H.E. Bass (2004). Atmospheric absorption in the atmosphere up to 160 km, *J.*
431 *Acoust. Soc. Am.* 115, 1012–1032, doi: 10.1121/1.1631937.

432 Waxler, R., J. Assink & D. Velea (2017a). Modal expansions for infrasound propagation and their
433 implications for ground-to-ground propagation, *J. Acoust. Soc. Am.* 141, 1290–1307, doi:
434 10.1121/1.4976067.

435 Waxler, R., J. Assink, C. Hetzer & D. Velea (2017b). NCPAprop—A software package for infrasound
436 propagation modeling. *J. Acoust. Soc. Am.*, 141, 3627, doi: 10.1121/1.4987797.

437

438

439 Table 1: Monthly statistics of the numbers of ARIANE engine tests detected or non-detected in the
 440 years 2000-2019, also giving the portion in each category. Note the total or nearly total lack of
 441 detections in May-September, or summer months, while the majority of engine test from October-
 442 April, or winter months, are observed.

443

Month	Det.		Non-Det.		Total
Jan	9	(69%)	4	(31%)	13
Feb	8	(73%)	3	(27%)	11
Mar	13	(76%)	4	(24%)	17
Apr	10	(56%)	8	(44%)	18
May	1	(8%)	12	(92%)	13
Jun	0	-	11	(100%)	11
Jul	0	-	21	(100%)	21
Aug	0	-	14	(100%)	14
Sep	1	(17%)	5	(83%)	6
Oct	8	(73%)	3	(27%)	11
Nov	10	(91%)	1	(9%)	11
Dec	11	(85%)	2	(15%)	13
Sum	71		88		159

444

445

446

447 Table 2: Detection statistics compared to effective sound speed ratio and stratospheric shadow zone. In
 448 each cell the first number is the count for those propagation models that show a stratospherically
 449 ducted path to IS26, while the second number gives the counts with a shadow zone. An asterisk
 450 indicates a case where the shadow zone is questionable (see also footnotes). For example, in the
 451 second column ($1.1 < v_{\text{eff-ratio}} < 1.2$) there are 9 good signal detections with a stratospheric path to the
 452 station, and one good detection, where the station is possibly within a shadow zone. Note: Of the 71
 453 observed signal detections 41 are predicted/confirmed by the ECMWF model with varying signal levels,
 454 while for 30 cases the station is predicted to be, or possibly be, within a shadow zone (see marked cells
 455 in "Row sum" column). With the benefit of doubt for the 5 cases of uncertainty (potentially resolved by
 456 using gravity wave perturbations) 46 explained cases are offset by 25 unexplained/shadow zone cases.
 457 Furthermore, there are 7 non-detections when the $v_{\text{eff-ratio}}$ is distinctly above 1, but not any associated
 458 shadow zone. For further discussion of the 20 non-detection cases within the framed cells, refer to
 459 Table 3.

460

	$v_{\text{eff-ratio}} > 1.2$	$1.1 < v_{\text{eff-ratio}} < 1.2$	$1 < v_{\text{eff-ratio}} < 1.1$	$0.98 < v_{\text{eff-ratio}} < 1$	$v_{\text{eff-ratio}} < 0.98$	Row sum
Detection(2)	25 / <u>0</u>	9 / <u>1</u>*	0 / <u>2</u>	-	-	34 / <u>3</u>*
Detection(1)	4 / <u>0</u>	1 / <u>6</u>*	0 / <u>4</u>*	- / <u>3</u>	-	5 / <u>13</u>^{2*}
Detection(0)	0 / <u>2</u>*	1 / <u>5</u>	1 / <u>6</u>*	- / <u>1</u>	-	2 / <u>14</u>^{2*}
Non-detection	<u>4</u> / 1	<u>3</u> / 6*	<u>0</u> / 6*	- / 9*	- / 59	<u>7</u> / 81^{3*}
Column total [# incon'cies] [‡]	36 [5]	32 [13]	19 [10]	13 [4]	59	159 [32]

461 *) 1 stratospheric shadow zone is questionable

462 ^{2*}) 2 stratospheric shadow zones are questionable

463 ^{3*}) 3 stratospheric shadow zones are questionable

464 [‡]) Number of inconsistencies, i.e. the underlined numbers above, but neglecting the cases of
 465 questionable shadow zones (marked by asterisks)

466

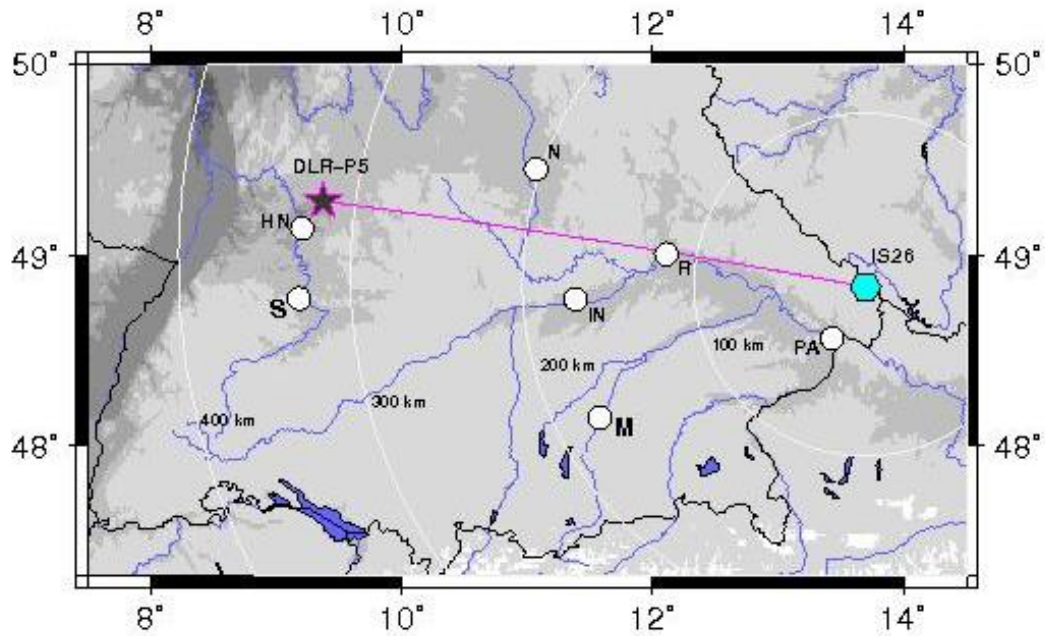
467

468 Table 3: List of ARIANE engine tests for which a stratospheric duct exists based on the atmospheric
 469 model (ECMWF) ($v_{\text{eff-ratio}} > 1$), but for which no signals could be identified at IS26. The highlighted entries
 470 (bold text) indicate those tests, where the propagation modeling does not produce a shadow zone at or
 471 near IS26, while for other entries such a shadow zone exists (even if doubtful, as indicated by a
 472 question mark).

Test [ID #]	Date [YYYY MM DD HH]	Shadow Zone	Effective Sound Speed Ratio
150	2015 12 10 11	N	1.298
004	2000 03 09 15	N	1.227
062	2002 03 15 14	N	1.225
058	2002 01 31 14	Y	1.218
172	2019 02 21 14	N	1.208
106	2006 11 14 13	Y	1.192
170	2019 01 17 14	Y	1.184
157	2018 01 22 12	N	1.152
052	2001 10 25 13	Y	1.148
029	2000 12 07 15	N	1.146
002	2000 01 21 16	N	1.141
173	2019 03 07 15	Y	1.124
064	2002 04 04 13	?	1.104
115	2009 10 14 14	Y	1.103
023	2000 10 09 14	Y	1.097
066	2002 04 26 14	Y	1.057
037	2001 04 05 13	Y	1.050
088	2004 04 16 13	Y	1.048
146	2015 09 28 13	Y	1.047
041	2001 05 04 12	?	1.007

473 **Figures:**

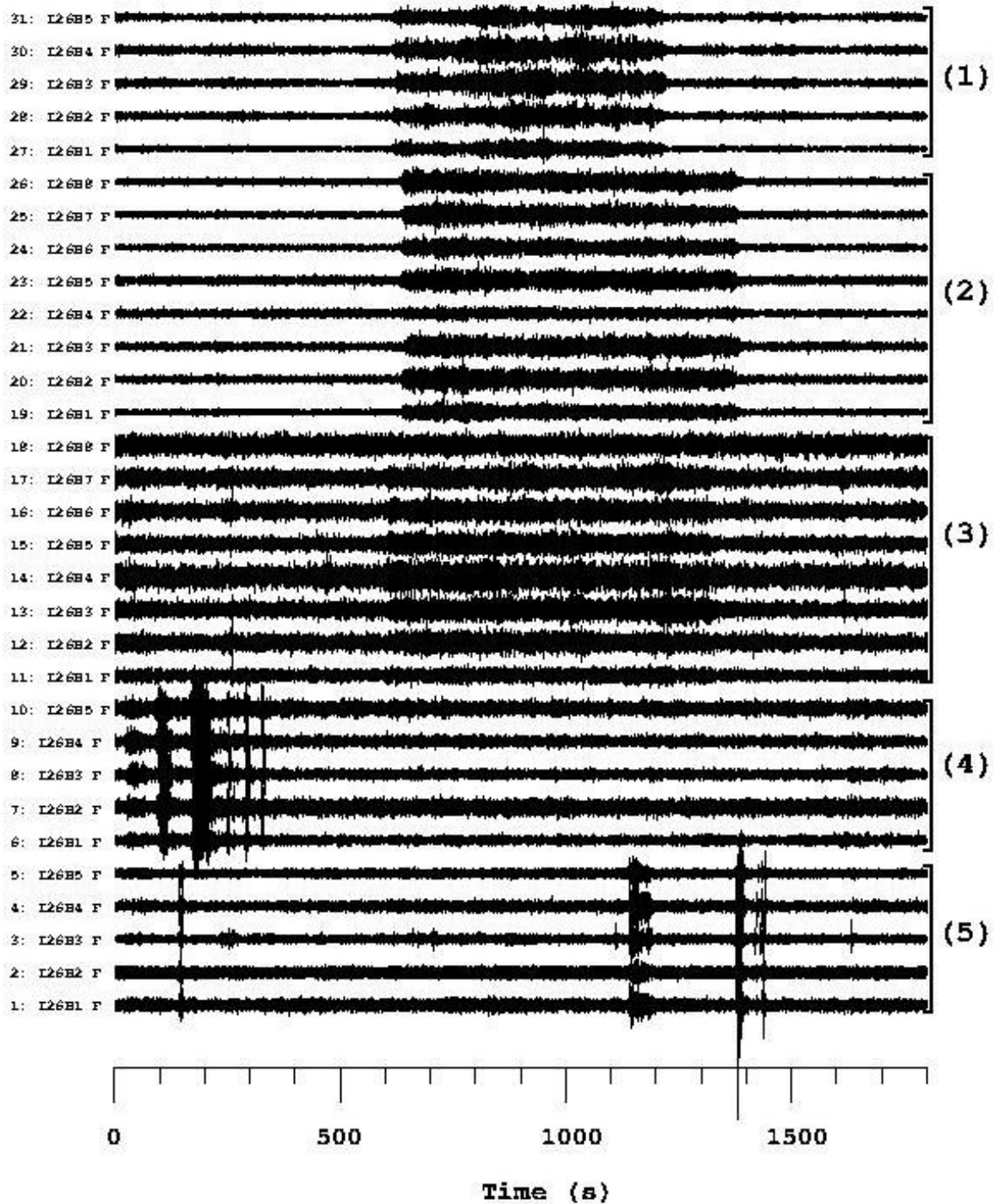
474



475

476 Fig.1: Geographical map showing the location of the propulsion test facility P5 of DLR (star) near
477 Heilbronn (denoted by HN label) and the IMS infrasound station IS26 (hexagon) in the Bavarian forest.
478 Distance circles in increments of 100km are also displayed, with IS26 at a range of 320 km and with a
479 backazimuth of 280° from the P5. Additionally, the locations of major cities in southern German are
480 given: Stuttgart (S), Nuremberg (N), Ingolstadt (IN), Munich (M), Regensburg (R), and Passau (PA).

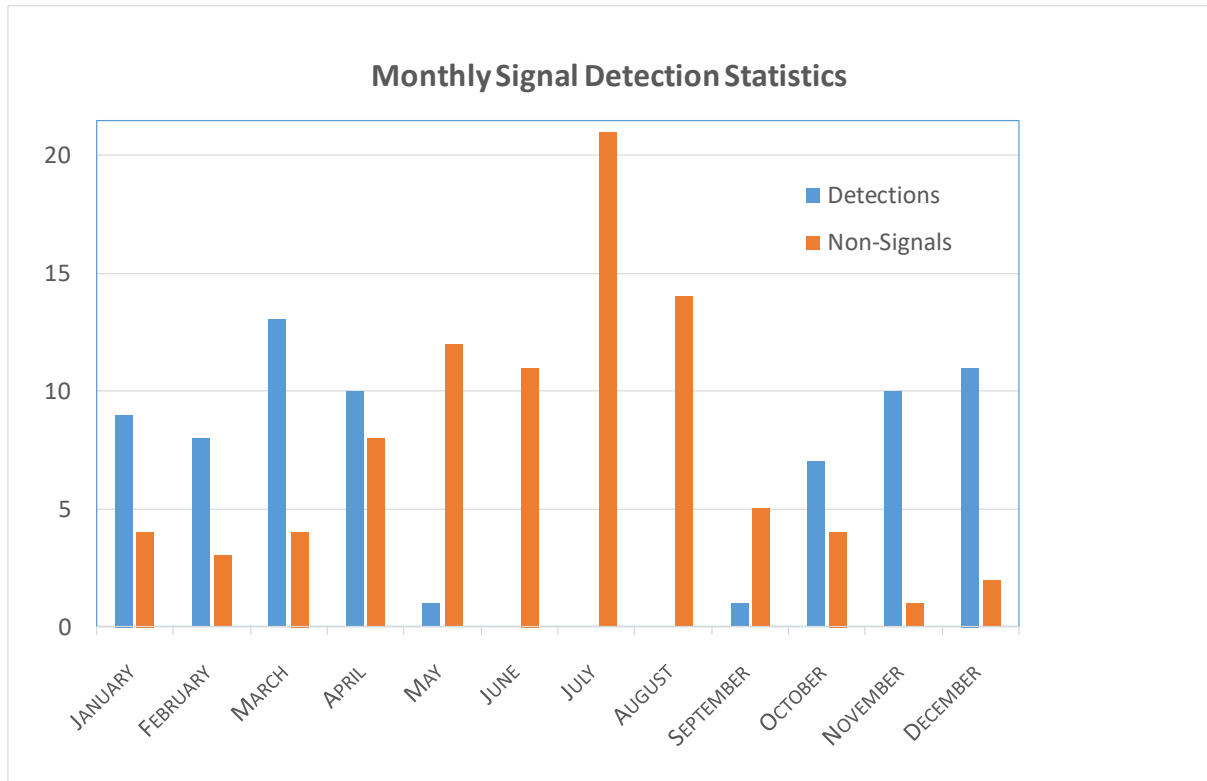
481



482

483 Fig.2: Waveform recordings of infrasound signals at IS26 for 5 ARIANE engine tests showing good
 484 signals for the top two events, fair to poor signals for the middle event, and no signals for the two
 485 bottom events (from top to bottom: (1) 23-Nov-2000, (2) 14-Feb-2013, (3) 16-Feb-2012, (4) 7-Dec-
 486 2000, (5) 3-Jul-2001). All engine tests had durations of more than 600 s, as can be deduced from the
 487 traces for the top three events.

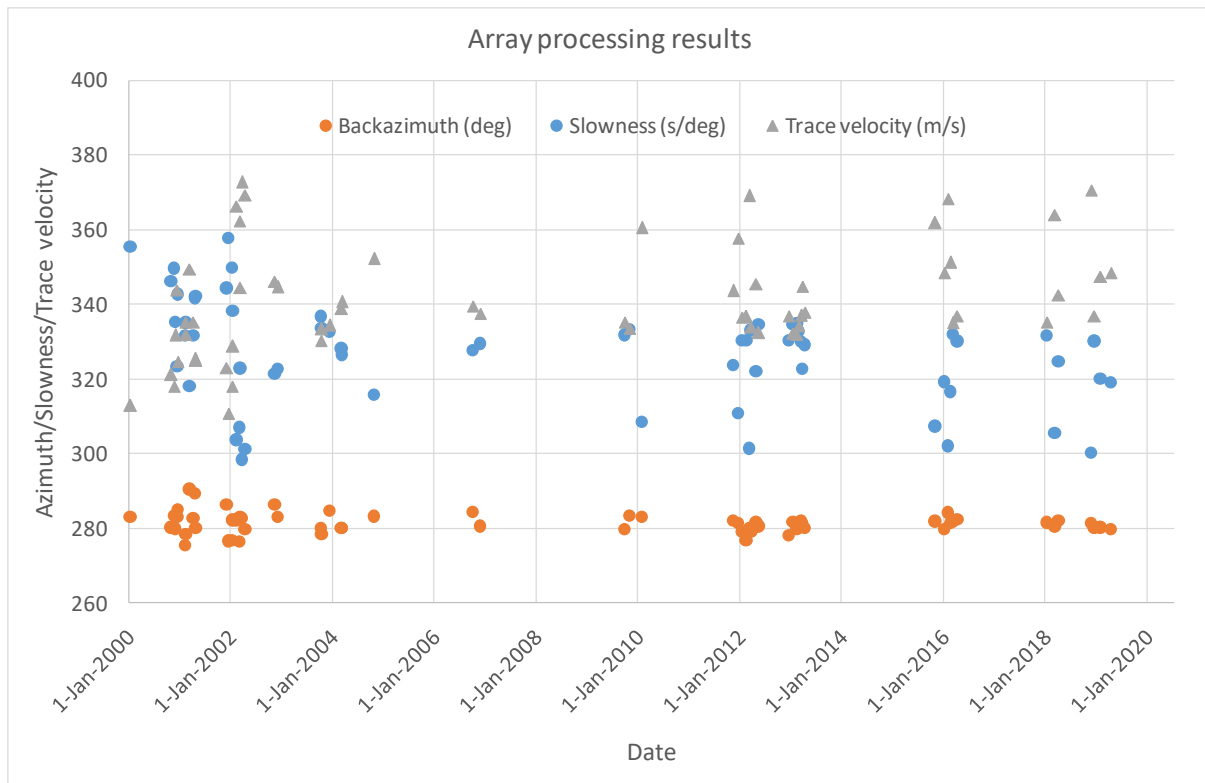
488



489

490 Fig.3: Monthly statistics on signal observations/detections and non-detections for the years 2000-
 491 2019, with the 70 detections being distributed almost exclusively between October and April (and not
 492 detections in Jun-Aug), while non-detections being mainly observed in summer, but rarely also during
 493 winter months.

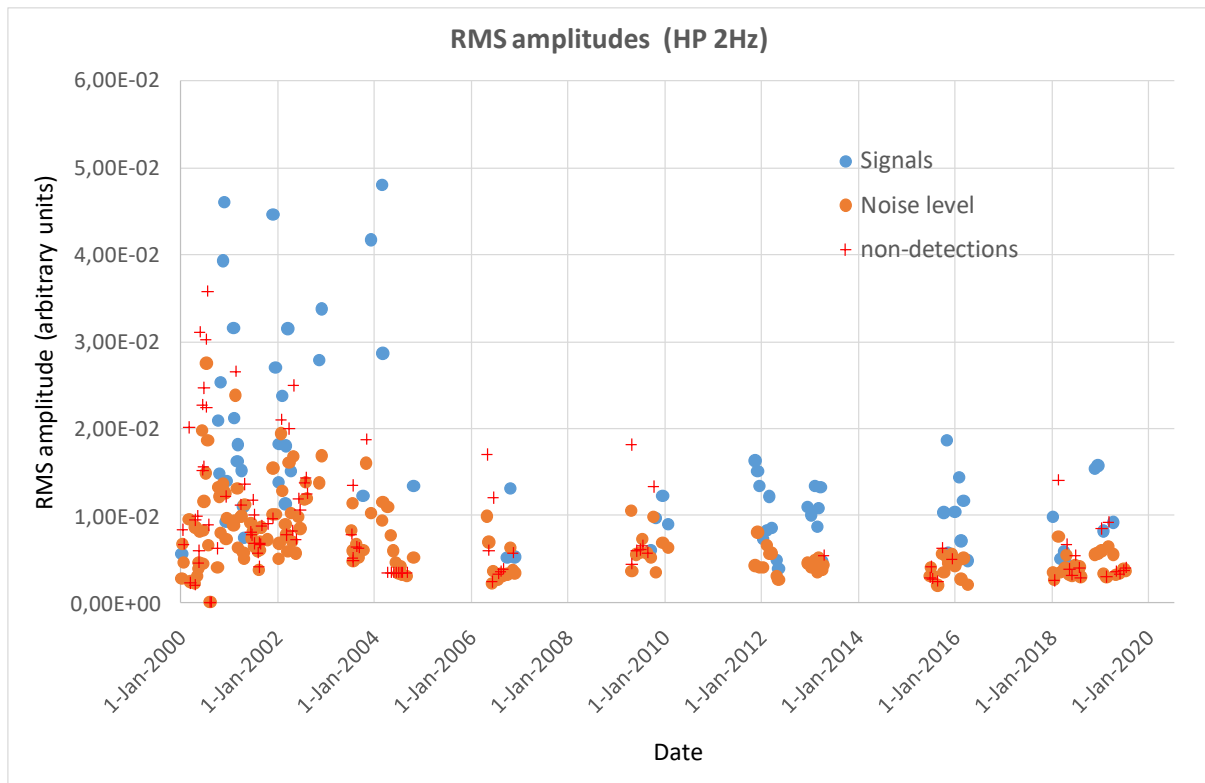
494



495

496 Fig.4: Results of the array data processing for the infrasound signals at IS26. The backazimuth scatters
 497 around the theoretical value by about $\pm 5^\circ$. The slowness estimate from FK analysis (i.e. output of the
 498 applied software) converted to apparent (or trace) velocity scatters between 310 and 370 m/s. Note
 499 the larger uncertainties before 2008, which may be related to the smaller number of five array
 500 elements compared to the present-day eight elements.

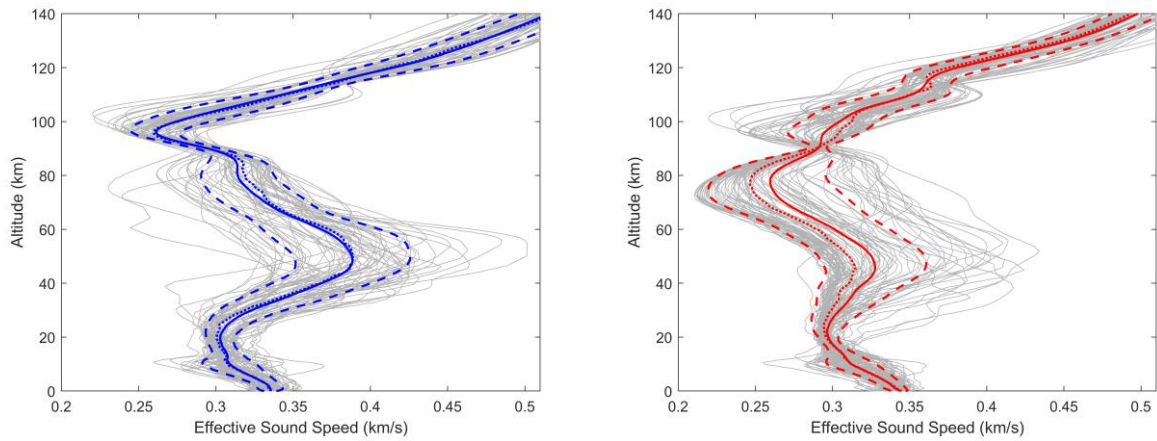
501



502

503 Fig.5: RMS amplitude measurements for signals (blue dots) and pre-signal noise levels (orange dots) for
 504 detection and noise levels for non-detections (red- crosses). Note the larger scatter prior to the year
 505 2004 propagation when impedance filters were installed at the infrasound station.

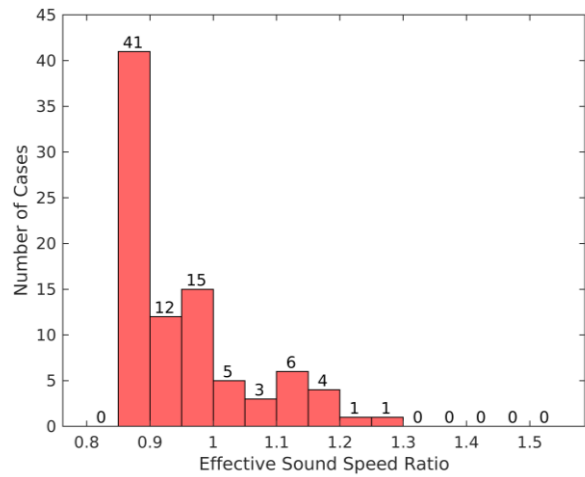
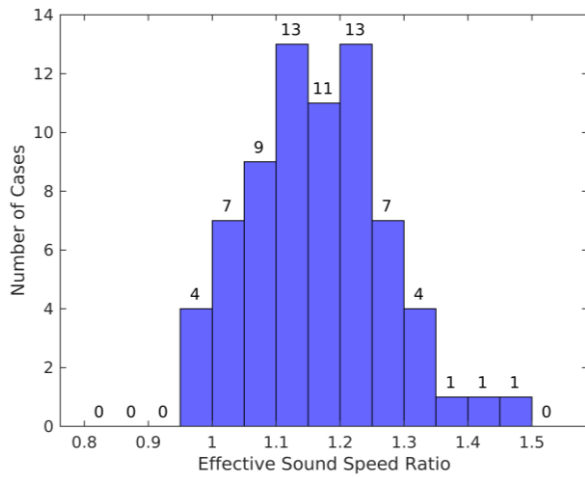
506



507

508 Fig.6: Effective sound speed profiles from the surface to an altitude of 140 km based on ECMWF
 509 models for time s of (a - left) signal detections, and (b - right) non-detections. From the individual
 510 models (gray lines) a mean (solid line) and median model (dotted line) was determined, as well as the
 511 associated standard deviations (dashed lines). For case (a) the mean and median models are nearly
 512 identical, while in the case of non-detections they are significantly different.

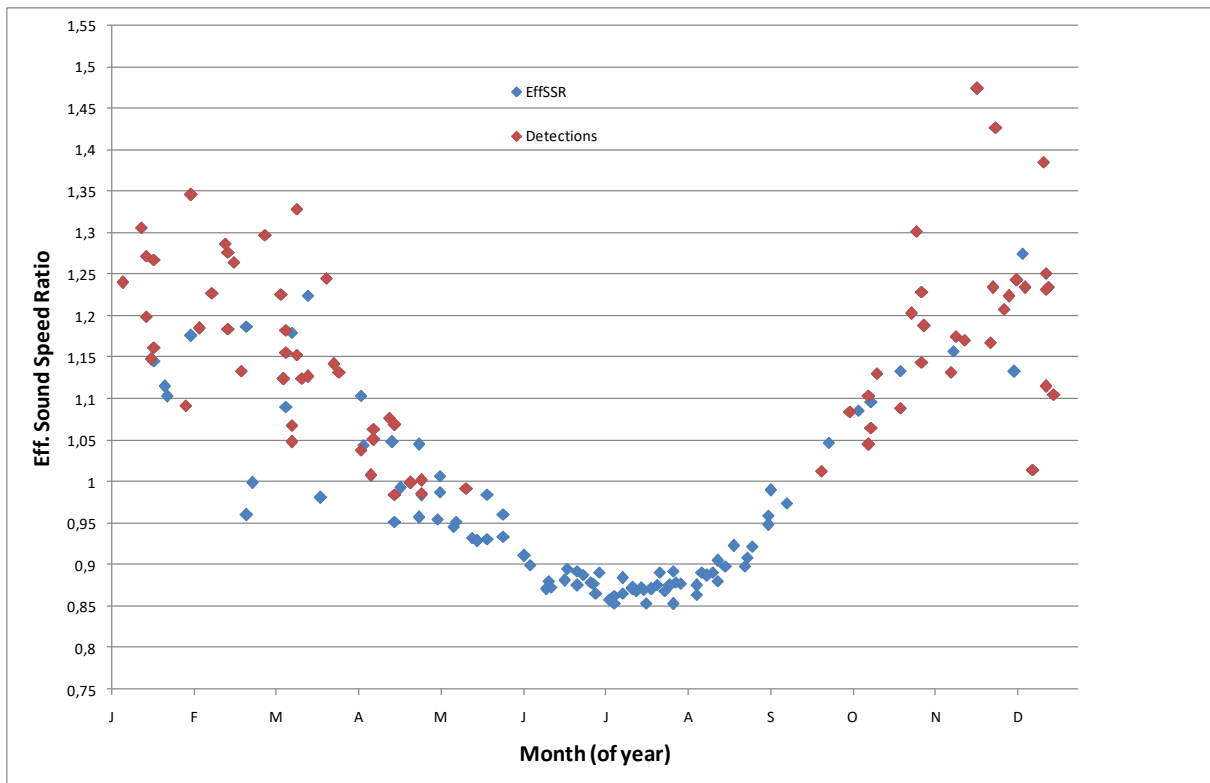
513



514

515 Fig.7: Histograms of the effective sound speed ratio of the ECMWF models for the cases with signal
 516 detections from ARIANE engines tests (a-left) and for cases for which no signals could be found (b-
 517 right). For signal detections, the $v_{\text{eff-ratio}}$ of the ECMWF models is larger than 1 except for four cases.
 518 For nearly half of tests it is between 0.85 and 0.9, but in 20 cases the $v_{\text{eff-ratio}}$ exceeds 1.0, indicative
 519 for the existence of a stratospheric duct.

520



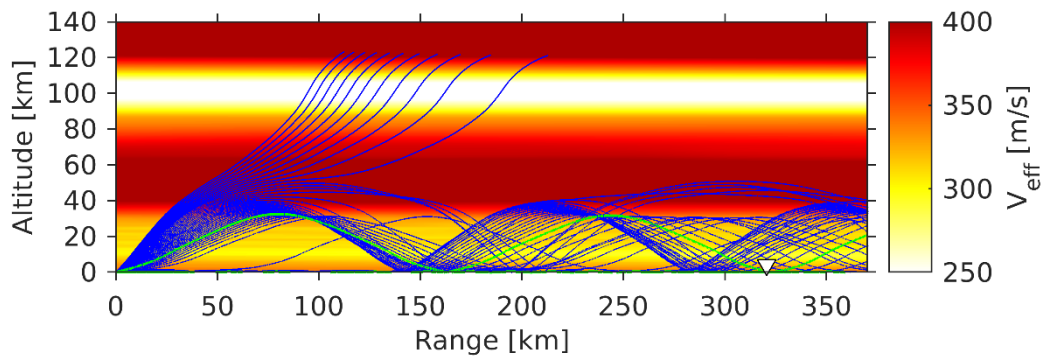
521

522 Fig.8: The effective sound speed ratios for the atmospheric models associated with the 71 signals
 523 detections and 88 non-detections. Cases with signal detections are marked with red symbols, while
 524 cases with non-detections are shown in blue. For the summer months June through August the v_{eff}
 525 ratio is fairly stable between 0.85 and 0.9 and associated with the lack of any detection. For the
 526 remained of the year, both detections and non-detections can occur.

527

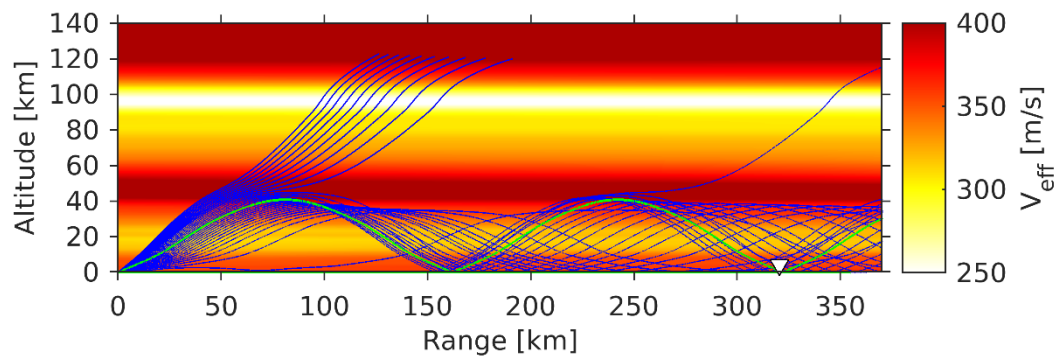
528

529 A) case150



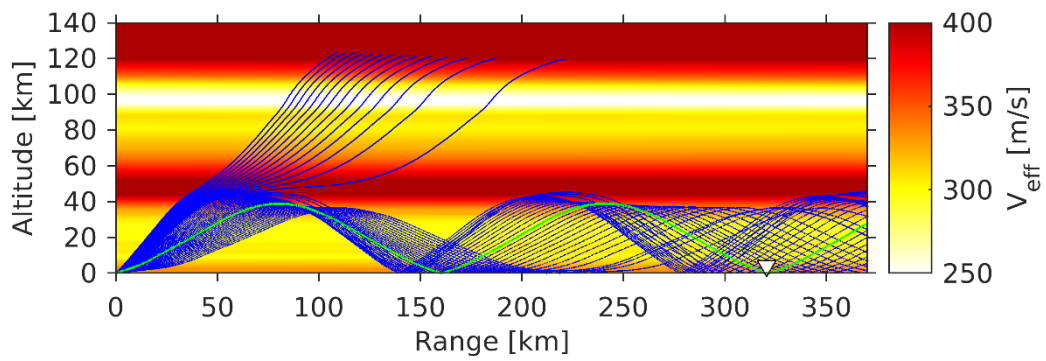
530

531 B) case004



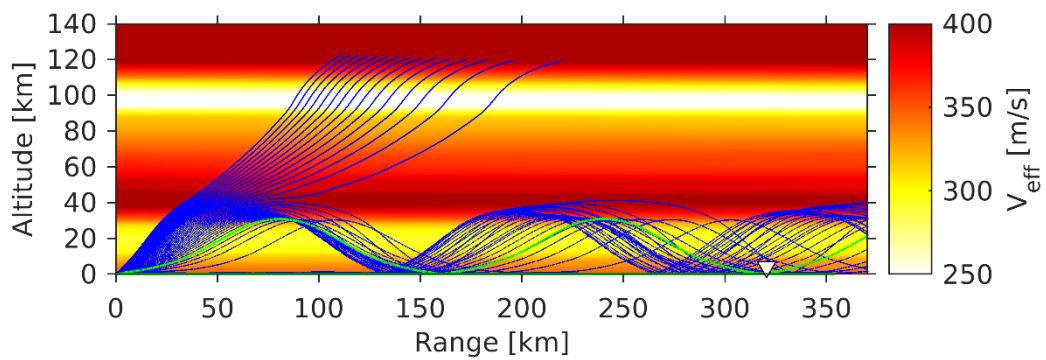
532

533 C) case062



534

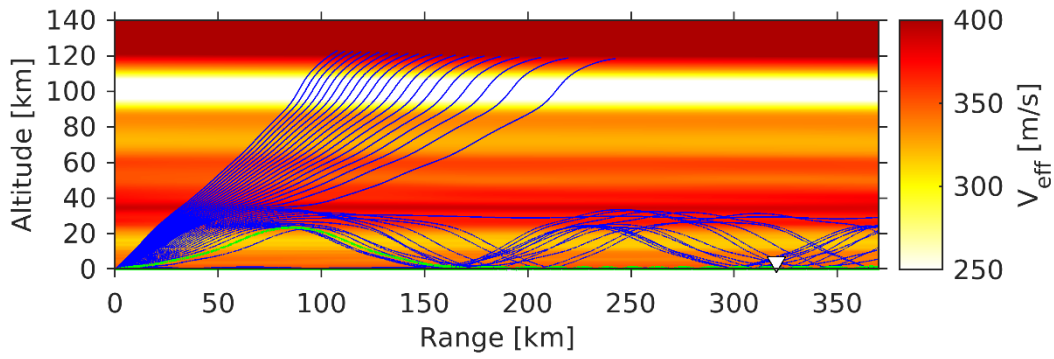
535 D) case172



536

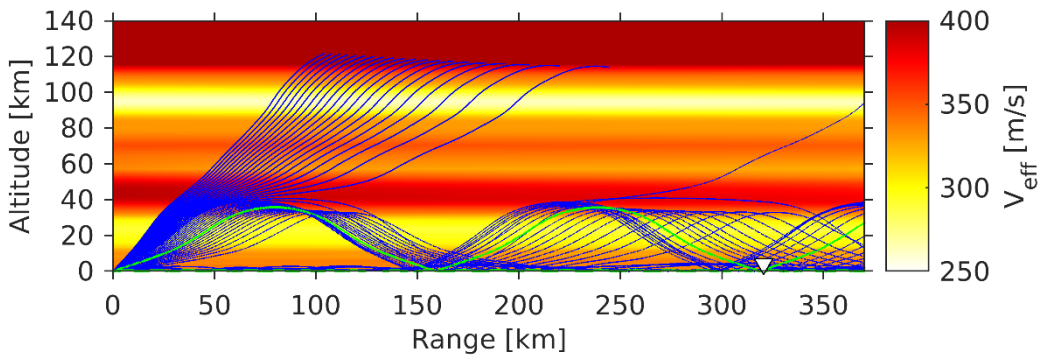
537 Fig.9 (cont'd)

538 E) case157



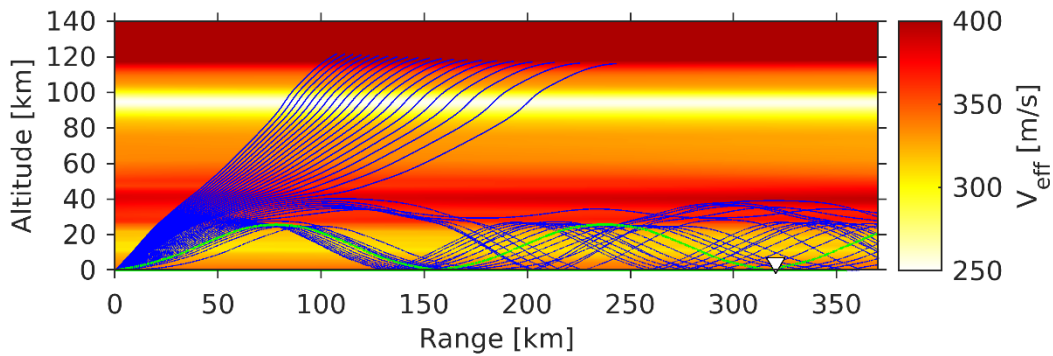
539

540 F) case029



541

542 G) case 002



543

544 Fig.9: Two-dimensional ray-trace propagation modeling between the DLR rocket engine test facility
545 (axes origin) and infrasound array IS26 (white triangle) for the 7 non-detection cases. ECMWF models
546 provide effective sound speed values (V_{eff} , color-coded) being larger than the effective sound speed
547 near the ground (thus effective sound speed ratio >1), showing a suitable stratospheric duct without a
548 shadow zone near the station.

549

550

Figure 1.

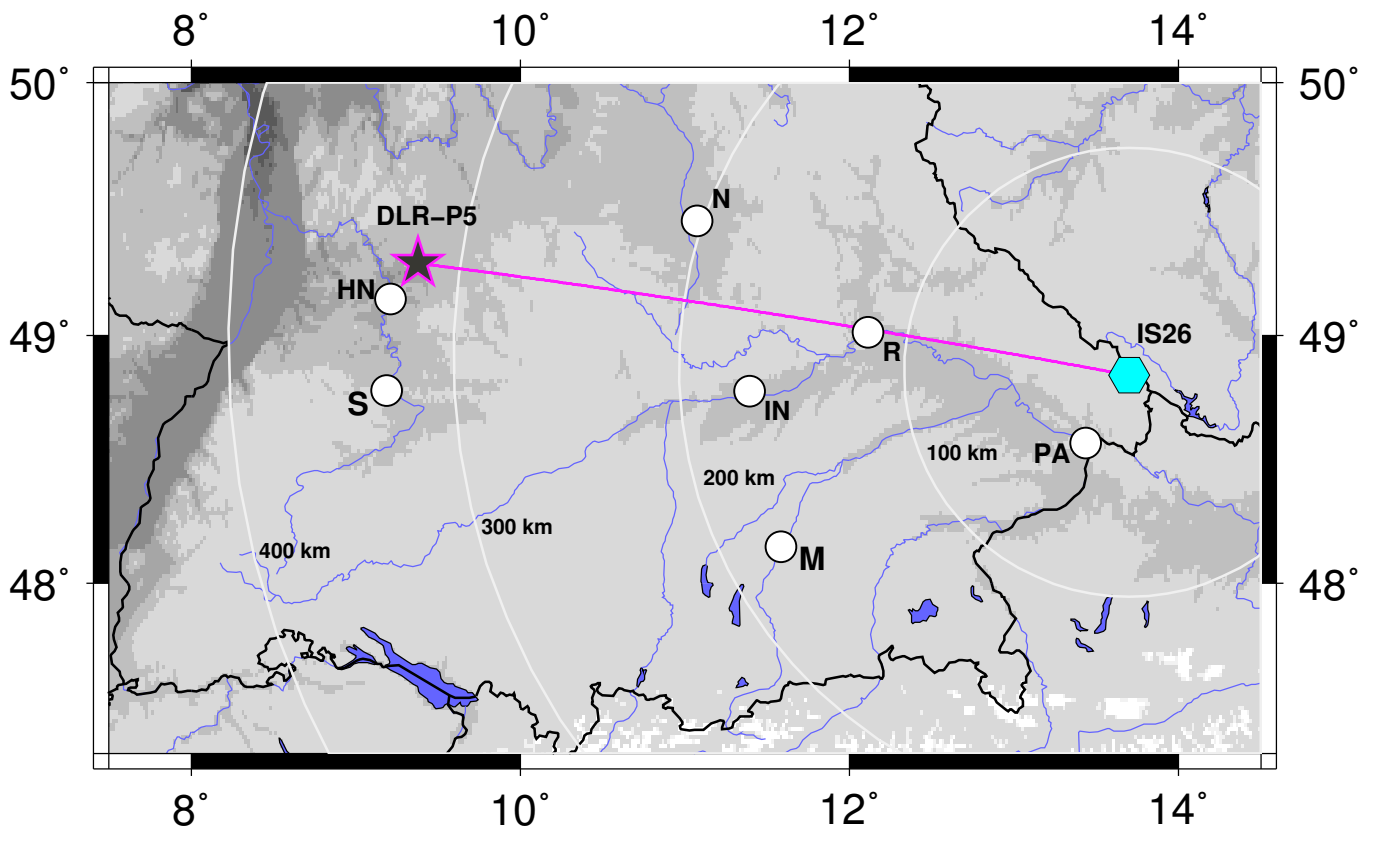


Figure 2 (small version).

